EPJ Web of Conferences **39**, 07004 (2012)
DOI: 10.1051/epjconf/20123907004

Tidal disruption of asteroids by supermassive black holes

U. Kostić[1,a], A. Čadež[1], M. Calvani[2], and A. Gomboc[1]

[1] *University of Ljubljana, Faculty of Mathematics and Physics, Jadranska 19, 1000 Ljubljana, Slovenia*
[2] *INAF – Astronomical Observatory of Padova, Vicolo Osservatorio 5, 35122 Padova, Italy*

Abstract. The compact radio source Sgr A* at the centre of our Galaxy harbours a super-massive black hole, and is therefore the nearest laboratory for testing the super-massive black hole astrophysics and environment. Since it is not an active galactic nucleus, it also offers the possibility of observing the capture of low-mass objects, such as comets or asteroids, that may orbit the central black hole. In this paper we discuss conditions for tidal disruption of low-mass objects and predictions of the appearance and light curve of such events, as well as their relevance for the X-ray and infra-red flares detected in Sgr A*. The modelled light curves of such tidal disruption events bear marks of the strong gravitational field: tidal squeezing and elongation of the object, gravitational lensing, aberration of light, and Doppler effects. Finally, we show that this model is able to reproduce and fit X-ray flares.

1. INTRODUCTION

The centre of our Galaxy harbours a massive black hole of mass $4 \times 10^6 M_\odot$ [1]. Although the black hole at the Galactic centre (GC) is not an active one, flares from its direction have been detected in X-rays and in infra-red. These flares typically last 50–100 min and are modulated on a short time-scale with average periods of 15–20 minutes [2–5]. Multiwavelength campaigns found that the time lag between X-ray and NIR flare emission is small, strongly suggesting a common physical origin [6–9]. It has been determined that the size of the emitting region is smaller than $6r_g$ [10], and if the emitted energy $E \geq 10^{39.5}$ erg comes from the potential energy differences, which in this region are expected to be of the order of a few percent of Mc^2, then the objects producing them probably have masses of the order of 10^{20} g [2].

In this paper we show, that these observational results can be explained with asteroid-like objects orbiting the central black hole.

First we review the conditions for tidal disruption of objects near a black hole, where we show the difference between gravity dominated and solid state forces dominated objects. We use numerical simulations to study the last stage of in-falling events, and apply a ray-tracing technique to calculate the corresponding observational signature. The results are then used to reproduce an observed X-ray flare.

2. TIDAL INTERACTION

Strong tidal effects are induced by the gravitational field of a black hole on objects that find themselves below their Roche radius, leading to tidal disruption and to the release of a large part of gravitational energy on short time-scales. The strength of the tidal force is described by the ratio of the Roche radius to the periastron distance, i.e. the Roche penetration factor $\beta = r_R/r_p$. If an object of mass M and radius R is held together by self gravity, the Roche radius r_R is

$$r_R \approx \left(\frac{M_{BH}}{M}\right)^{1/3} R, \tag{1}$$

where M_{BH} is the mass of the black hole. If, however, the object is dominated by solid state forces, it can resist the strong tidal forces much more effectively, thus pushing its Roche radius closer to the black hole. In this case, the Roche radius can be approximated as [11, 12]

$$r_R \approx 10 r_g \left(\frac{1}{2\pi}\frac{R}{r_g}\frac{c}{c_s}\right)^{2/3}, \tag{2}$$

where $r_g = GM_{BH}/c^2$ is the gravitational radius, c is the speed of light, and c_s is the speed of sound (which depends on the object's density and elasticity). Taking some typical values for asteroids, it turns out that the radius dividing the two classes is between 200–300 km, which is the radius of the asteroid Vesta.

For the black hole from the Galactic Centre, these conditions are illustrated in Fig. 1, where the Roche radius is plotted as a function of the object's size for different masses for gravity dominated and solid state dominated objects. This figure shows that gravity dominated satellites, orbiting a super-massive black hole, start rapid tidal evolution when their periastron reaches $r_p \approx 10r_g$, while solid state dominated bodies may start significant tidal evolution even closer to the black hole. Actually, the Roche radius for most solid asteroids is below $2r_g$, so these asteroids cannot get tidally disrupted at all.[1]

However, as tidal work is done on the satellite, it melts on a thermal diffusion time-scale $\tau_{Th} = R^2\pi^{-2}D^{-1}$, which is of the order of 3×10^5 years for 10 km objects consisting of solid rock [11, 13].[2] Because melting weakens the

---

[a] e-mail: `uros.kostic@fmf.uni-lj.si`

[1] Perhaps it is worth mentioning that there are moons in our Solar system, which orbit their planets below the gravitational Roche radius (1). Obviously, they are not tidally destroyed because of their solid state nature.

[2] Evidence of such tidal heating and melting of the interior of a satellite can be found in our Solar system.

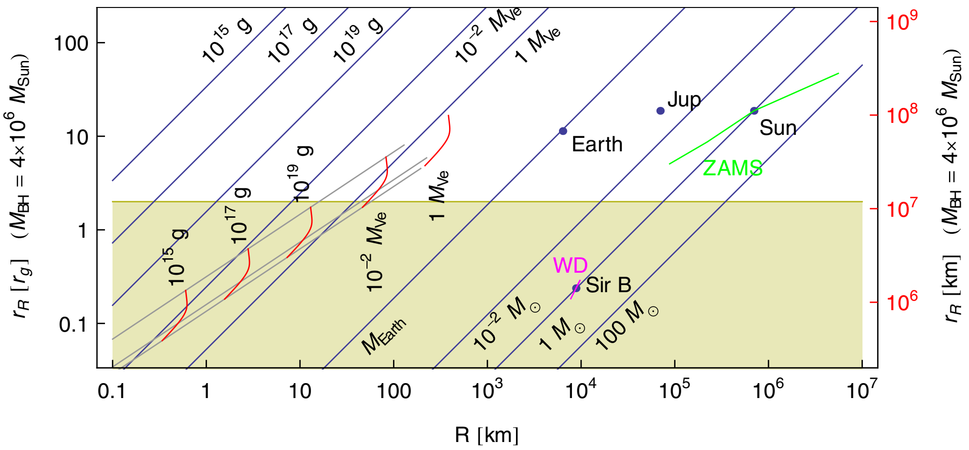

Figure 1. Roche radius as a function of mass and radius of the object for a super-massive black hole with $M_{BH} = 4 \times 10^6 M_\odot$. Blue lines show Roche radius for gravity dominated objects and red lines for solid state dominated objects (M_{Ve} is the mass of the asteroid Vesta). Lines of constant speed of sound c_s are plotted in light grey and refer to $c_s = 1.5, 3.5, 5\,\mathrm{km\,s^{-1}}$ (ice, rock, iron). Some celestial objects are marked by blue dots: Earth, Jupiter, Sun, and Sirius B. The green line represents zero age main sequence stars and the purple line represents white dwarfs. The shaded area below yellow line marks the radii below $2r_g$.

structure of solid objects, the objects that were orbiting the black hole below the gravitational Roche radius but well above their solid-state Roche radius (e.g. $r_p \sim 10r_g$), are no longer resistant to tidal forces, and can be consequently tidally disrupted.

3. TIDAL DISRUPTION AND X-RAY FLARES

The last stages of tidal capture of such small melted object orbiting a Schwarzschild black hole are studied here. To make calculations manageable, the problem is simplified in the following way: Consider a solid spherical object moving around a black hole. When tidal forces do enough work, it momentarily melts. After this moment, pressure forces become negligible with respect to inertial forces and the particles that constitute the object start to fall freely in the gravitational field of the black hole. A ray-tracing procedure [14] from points on the object's surface to the distant observer is used to determine its appearance and light curve. The resulting light curves are then used to fit an observed X-ray flare from Sgra A*.

3.1. Numerical code

The calculations start with a spherical object, far from the black hole. The surface of this object is triangulated with respect to the mesh of spherical coordinates on the original sphere. Before melting, the sphere is considered as rigid and non-rotating. Its centre of mass follows an almost parabolic time-like geodesic. The coordinates of mesh points are expressed in the Fermi-Walker transported frame local to the centre of mass and are initially constant with respect to proper time. The rigidity constraint prescribes the same velocity for each point on the sphere. When the sphere is melted, the constraint no longer applies and surface mesh points start following time-like geodesics specified with their inherited energy and angular momentum (different for each mesh point).

The object is considered as a monochromatic radiator emitting according to Lambert's law in its own rest frame. The image of the object is constructed by mapping triangles on the surface of the object onto the image plane of the observer and assigning the appropriate intensity and frequency to their image. Through gravitational lensing, each vertex on the object produces multiple images. Because the size of higher order images exponentially decreases with order, it is sufficient to take into account only the primary and secondary image [15]. The image is observed in the image plane at constant time intervals with respect to the observer. Since we are dealing with a highly dynamical problem, we also take into account that light travel times from the object to the observer are different for rays from different vertices.

3.2. Results

The images of one such in-falling event at different observer's times are shown in Fig. 2 and the resulting light-curve in Fig. 3. The orbit of the object was chosen so that it makes about three to four turns around the black hole at $r = 4r_g$ before falling into it, and the observer was located 5° above the orbital plane. To compare light-curves with orbiting objects of fixed size (e.g. solid asteroids), we also show in Fig. 3 the light curve of a freely falling rigid object.

The sharp and narrow peaks in the light-curve are due to gravitational lensing and always come in pairs: the lower one is the contribution of the secondary image and precedes the one from the primary image. The peaks are higher and sharper if the observer is closer to the orbital plane. In this case parts of Einstein ring are observed. The wider bumps following sharp peaks are the result of Doppler boosting and aberration beaming of light. Since the object circles the black hole approximately three times before falling into it, three to four peaks in the light-curve can be observed. The overall increase in luminosity is a consequence of the exponentially growing surface of

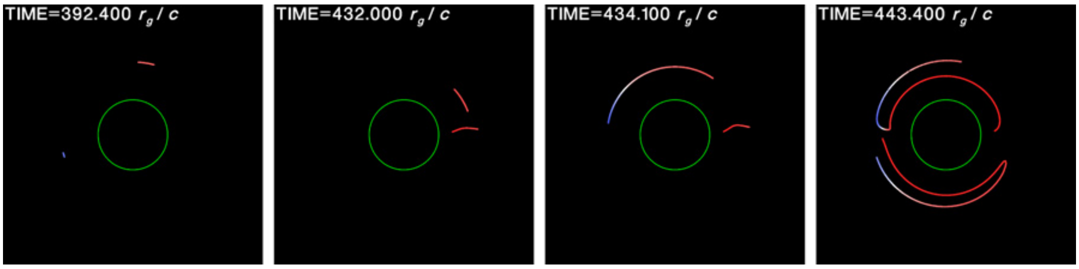

Figure 2. The image of a melted object that was initially spherical. The colours correspond to the redshift. The green circle represents the Schwarzschild radius.

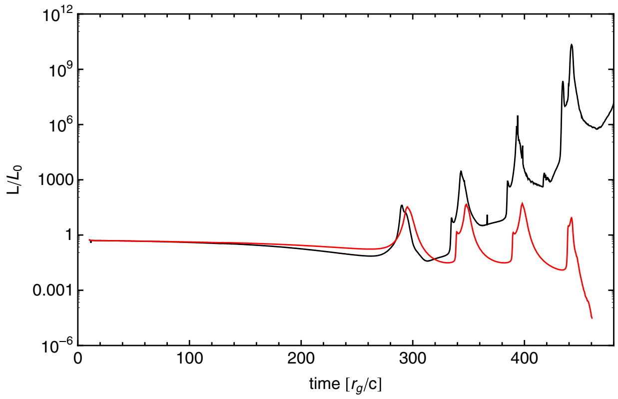

Figure 3. Light-curve of an initially spherical object of size $10^{-5}r_g$. The light-curve of melted object is in black, and of rigid sphere in red.

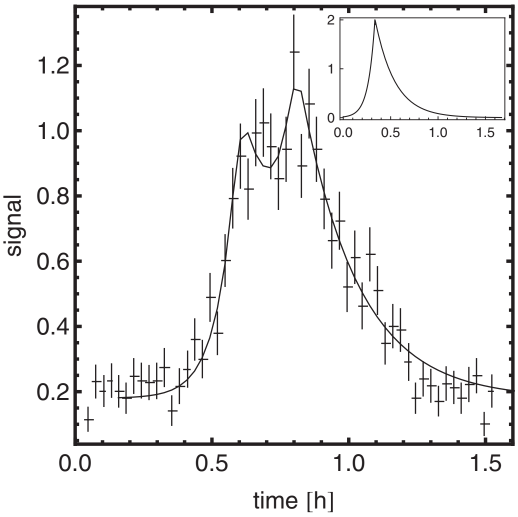

Figure 4. The XMM-Newton/EPIC light curve of the flare of April 4, 2007 [16], fitted with the simple intensity distribution shown in the inset at top right.

the object, while it stretches into an elongated, spiral-like structure.

3.3. A simple scenario for X-ray flares

Taking into account the characteristic of X-ray flares, the following crude scenario can be constructed.

Consider an object on a highly eccentric orbit with periastron below $\sim 10r_g$, where it melts due to the tidal force. Let us assume that the energy released during this process comes from the gravitational potential energy of the object and is thus proportional to its mass. Since potential energy differences on a low periastron orbit are of the order of a few percent of Mc^2, it follows that objects producing the flares probably have masses of the order of 10^{20} g. If the source of flares is some sort of a gaseous blob with such large mass, it finds itself below the Roche radius far from the black hole and is therefore completely disrupted before producing any modulation of the light curve. Therefore, the source of the flares is small and initially solid object, which eventually melts in the close vicinity of the black hole.

After the tidal deformation develops, the deformed object can be imagined as a long string of freely falling smaller pieces threading the same orbit. The light-curve $S(t)$ of such a string can be described by a convolution

$$S(t) = \int G(t,t')K(t')dt', \tag{3}$$

where $G(t,t')$ is the Green's function belonging to the orbit and is dominated by a series of sharp spikes produced during the last few turns before plunging behind the horizon (i.e. it is the signal, as a function of time t, of a single small piece crossing a fixed reference point at time t'), while $K(t')$ is the distribution of luminosity among the small pieces.

We use the observed signal $S(t)$ and solve (3) for the luminosity distribution $K(t')$. Depending on the Green's function used, different solutions are obtained, most of which are physically unrealistic highly variable functions. In case of the XMM-Newton/EPIC light curve of the X-ray flare of April 4, 2007 [16], only for orbital angular momentum $l/mr_gc = 4.3$ and orbital energy $E = 1.04mc^2$ does the distribution become a simple positive function, which can be well approximated with a steep, exponential rise, followed by a slower, exponential decay. Both, the fitted light-curve and the luminosity distribution are shown in Fig. 4.

The function $K(t')$ and the Green's function described above thus represent a viable description of a flare produced by an originally small object that is tidally distorted into a long thread during the last exponential part of its tidal evolution.

4. SUMMARY

The strength of the tidal interaction depends not only on the distance of the object from the black hole, but also on the structure of the orbiting object. If the object is dominated by solid state forces, its Roche radius is much closer to the black hole than the Roche radius of a gravity dominated object. Although solid objects can resist the strong tidal forces more effectively than gravity dominated ones, the tidal interaction can melt them and thus make them more susceptible to the tidal deformations. In fact, as soon as they are melted, they can be tidally disrupted or destroyed, if they orbit the black hole below the (gravitational) Roche radius.

The light-curves calculated in simulations of the last stages of an in-fall of such an object show characteristic sharp peaks due to relativistic effects and an overall increase in luminosity due to growing tidal deformation. The time-scales of modulations of the calculated light-curves correspond to orbital time-scales at few gravitational radii, and have a coherence which is in agreement with observations. The comparison of the light-curves with the observed ones, the energies involved, and the time-scales suggest that tidal interaction may well be responsible for the NIR/X-ray flares from Sgr A*. In fact, using the above results, we successfully reproduced the XMM-Newton/EPIC light-curve of the flare of April 4, 2007.

References

[1] A.M. Ghez, S. Salim, N.N. Weinberg, J.R. Lu, T. Do, J.K. Dunn, K. Matthews, M.R. Morris, S. Yelda, E.E. Becklin et al., ApJ **689**, 1044 (2008)

[2] R. Genzel, R. Schödel, T. Ott, A. Eckart, T. Alexander, F. Lacombe, D. Rouan, B. Aschenbach, Nature **425**, 934 (2003)

[3] G. Bélanger, R. Terrier, O.C. de Jager, A. Goldwurm, F. Melia, Journal of Physics Conference Series **54**, 420 (2006)

[4] A. Eckart, R. Schödel, L. Meyer, S. Trippe, T. Ott, R. Genzel, A&A **455**, 1 (2006)

[5] L. Meyer, A. Eckart, R. Schödel, W.J. Duschl, K. Mužić, M. Dovčiak, V. Karas, A&A **460**, 15 (2006)

[6] A. Eckart, F.K. Baganoff, M. Morris, M.W. Bautz, W.N. Brandt, G.P. Garmire, R. Genzel, T. Ott, G.R. Ricker, C. Straubmeier et al., A&A **427**, 1 (2004)

[7] A. Eckart, F.K. Baganoff, R. Schödel, M. Morris, R. Genzel, G.C. Bower, D. Marrone, J.M. Moran, T. Viehmann, M.W. Bautz et al., A&A **450**, 535 (2006)

[8] F. Yusef-Zadeh, H. Bushouse, C.D. Dowell, M. Wardle, D. Roberts, C. Heinke, G.C. Bower, B. Vila-Vilaró, S. Shapiro, A. Goldwurm et al., ApJ **644**, 198 (2006)

[9] S. Trippe, T. Paumard, T. Ott, S. Gillessen, F. Eisenhauer, F. Martins, R. Genzel, MNRAS **375**, 764 (2007)

[10] M.J. Reid, International Journal of Modern Physics D **18**, 889 (2009)

[11] A. Čadež, M. Calvani, U. Kostić, A&A **487**, 527 (2008)

[12] S.S. Kokarev, Nuovo Cimento B Serie **124**, 155 (2009)

[13] U. Kostić, A. Čadež, M. Calvani, A. Gomboc, A&A **496**, 307 (2009)

[14] A. Čadež, U. Kostić, Phys. Rev. D **72**, 104024 (2005)

[15] A. Čadež, A. Gomboc, A&AS **119**, 293 (1996)

[16] D. Porquet, N. Grosso, P. Predehl, G. Hasinger, F. Yusef-Zadeh, B. Aschenbach, G. Trap, F. Melia, R.S. Warwick, A. Goldwurm et al., A&A **488**, 549 (2008)